

---

# Self-Supervised Structure-from-Motion through Tightly-Coupled Depth and Egomotion Networks

---

**Brandon Wagstaff\***

Institute for Aerospace Studies  
University of Toronto  
Toronto, ON, Canada  
brandon.wagstaff@mail.utoronto.ca

**Valentin Peretroukhin**

Computer Science and Artificial Intelligence Laboratory  
Massachusetts Institute of Technology  
Cambridge, MA, USA  
valentinp@csail.mit.edu

**Jonathan Kelly<sup>†\*</sup>**

Institute for Aerospace Studies  
University of Toronto  
Toronto, ON, Canada  
jkelly@utias.utoronto.ca

## Abstract

Much recent literature has formulated structure-from-motion (SfM) as a self-supervised learning problem where the goal is to jointly learn neural network models of depth and egomotion through view synthesis. Herein, we address the open problem of how to optimally *couple* the depth and egomotion network components. Toward this end, we introduce several notions of coupling, categorize existing approaches, and present a novel *tightly-coupled* approach that leverages the interdependence of depth and egomotion at training *and* at inference time. Our approach uses iterative view synthesis to recursively update the egomotion network input, permitting contextual information to be passed between the components without explicit weight sharing. Through substantial experiments, we demonstrate that our approach promotes consistency between the depth and egomotion predictions at test time, improves generalization on new data, and leads to state-of-the-art accuracy on indoor and outdoor depth and egomotion evaluation benchmarks.

## 1 Introduction

Structure-from-motion (SfM), the recovery of 3D scene structure and camera motion from a set of monocular images, is a fundamental component of vision-based state estimation for mobile robotics, autonomous driving, and augmented reality systems. Recently, learning-based SfM solutions have emerged that attempt to improve the overall accuracy and robustness of conventional techniques. Generally, these data-driven methods use convolutional neural networks (CNNs) to parameterize a direct mapping from pixel space to scene depth and camera motion. To train these networks, the self-supervised loss formulation [50] has become increasingly popular since it obviates the requirement for ground truth labels and can facilitate online adaptation. Without ground truth, the self-supervised training signal is generated by minimizing the photometric difference between a given ‘target’ image and a virtual image synthesized by warping a nearby source view using estimated scene depth and a relative camera pose (egomotion). Although this approach intimately ties depth and egomotion estimation, parameterizing both tasks through a single neural network has been shown to result in

---

\*Space & Terrestrial Autonomous Robotic Systems (STARS) Laboratory at the University of Toronto Institute for Aerospace Studies (UTIAS)

<sup>†</sup>Jonathan Kelly is a Vector Institute Faculty Affiliate.

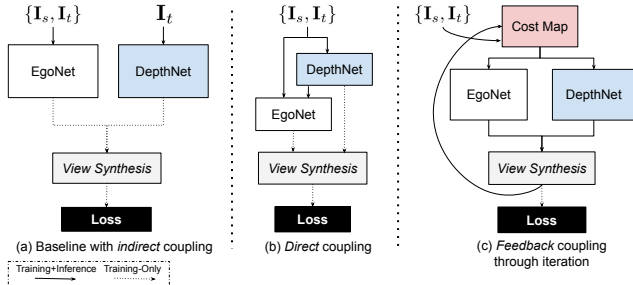


Figure 1: The three primary forms of coupling that exist between depth and egomotion networks. We demonstrate that feedback coupling is an effective form of coupling that reformulates the input as a cost map that is iteratively updated.

Method	Inference-time Coupling		
	Indirect	Direct	Feedback
Baseline [50, 13, 15]	—	—	—
PFT	—	—	—
[49, 5, 24, 27, 34, 20]	✓	—	—
Ambrus et al. [1]	—	D→E	—
ManyDepth [44]	✓	E→D	—
Nabavi et al. [28]	—	D→E	✓
DRO [14]	—	D⇌E	✓
Ours	✓	D→E	✓

Table 1: Summarizing the degree of coupling between depth and egomotion that are retained at inference time. Ours is the only method that uses all three forms of coupling.

inferior performance [13]. Two separate networks, however, must be *coupled* (i.e., linked) in some manner that results in generalizable estimates of depth and egomotion with mutually consistent notions of scale.

In this paper, we investigate and improve upon existing methods to achieve this coupling. First, we survey the field and categorize the approaches to coupling described in the literature (Figure 1 and Table 1). We find that most systems rely on *indirect coupling* of depth and egomotion via the self-supervised reconstruction loss; others incorporate *direct coupling* by treating one prediction as a function of the other [42, 23]; and lastly, a final set of methods [28, 14] incorporate a form of direct coupling we call *feedback coupling* to iteratively refine predictions based on successive forward passes.

Building on this taxonomy, we present a novel network structure that ensures the depth and egomotion network predictions are *tightly coupled* at both training and inference time by incorporating all three coupling strategies. Our approach leverages two specific methods — namely, test-time optimization [49, 5, 44, 24, 27, 34, 20] for parameter fine-tuning (PFT), and iterative view synthesis [28] to recursively update the egomotion network input with the most recent synthesized view. Through extensive experiments, we demonstrate that our approach promotes consistency between the depth and egomotion predictions at test time, improves generalization on new data, and leads to state-of-the-art accuracy on indoor and outdoor depth and egomotion evaluation benchmarks.

## 2 Related work

**Self-supervised depth and egomotion estimation:** Zhou et al. [50] initially showed that depth and egomotion networks can be trained by minimizing a photometric reconstruction loss. In this self-supervised training pipeline, the predicted depth and egomotion are used to differentially warp a (nearby) source image to reconstruct the target image. Building upon [50], recent works have improved the overall accuracy of the system through auxiliary loss terms [3, 26, 33], robust feature-metric losses [48, 34], novel network architectures [15, 1, 42], and techniques to mask out unstable pixels that break the photometric consistency assumptions [13, 4, 21]. In what follows, we attempt to broadly categorize the degree of coupling that exists between depth and egomotion in these systems.

**Indirect coupling** The majority of self-supervised methods [50, 13, 15, 22, 3, 26, 38] treat depth and egomotion as separate tasks, and consequently employ separate depth and egomotion networks (see Figure 1a). During training, the independently-estimated predictions are coupled as part of the view synthesis procedure, which uses depth and egomotion to reconstruct the target view from a nearby source view. We call this *indirect* coupling because there is no explicit linking of depth and egomotion; rather, the weights of each network are coupled through gradient flow alone. Although this form of coupling is sufficient to jointly learn depth and egomotion, the major drawback is that the networks become decoupled at test time, which prevents contextual information (such as scale) from being passed from one network to the other. Recently, however, it has been proposed that — owing to its self-supervised nature — the reconstruction loss can be retained at inference time, and be further minimized by a gradient-descent-based optimizer [49, 5, 44, 24, 27, 34, 20]. In doing so,

the indirect link between networks (via gradient flow from the loss function) is preserved at inference time. Further, by retaining the indirect coupling at test time, multiview geometry constraints can be enforced by minimizing the error from multiple source images. To do this, there are two general strategies: parameter fine-tuning (PFT), which further optimizes the network weights, and output fine-tuning (OFT), which directly optimizes depth or egomotion predictions.

**Direct coupling** Beyond the basic coupling within the loss function, other methods promote consistency between depth and egomotion by explicitly linking depth and egomotion within the network structure. Some methods [40, 13] use weight sharing to merge the network structures; however, we note that Godard et al. [13] report that a baseline “shared” network structure was less accurate than a system with independent networks. Other methods [42, 23, 1, 51] estimate egomotion as a function of the predicted depth (see Figure 1b), with [1, 51] providing ablation studies indicating that doing so improves accuracy. Less commonly, egomotion predictions have been used to directly aid in the estimation of depth [44, 41].

**Feedback coupling** Feedback coupling is a method that enables network *introspection* by reformulating its own input as a cost map built with the current depth and egomotion predictions (see Figure 1c). Doing so explicitly encodes error within the input, which networks can utilize by iteratively updating the current prediction (i.e., through multiple forward passes). As the predictions improve, the cost map is updated, and this process is repeated until convergence (i.e. until the cost map is minimized). We identify two existing self-supervised feedback coupling methods in the literature. Nabavi et al. [28] use a photometric cost map consisting of the target view, and a synthetic target view (generated from a nearby source view); optimal depth and egomotion predictions maximally align the synthesized view with the target view, which effectively minimizes the cost map. The authors of Deep Recurrent Optimizer (DRO) [14] adopt a similar approach, but replace the photometric cost map with a feature-metric one; further, they train separate (iterative) depth and egomotion “optimizers” that take as input the feature-metric cost map. Although DRO is able to jointly refine both depth and egomotion, they rely on a complicated training scheme that alternately updates one optimizer, while fixing the weights of the other. Other methods [45, 35, 36, 37, 6] use iteration for feedback coupling, but require supervision to train the relatively complex network structures. Herein, we demonstrate that feedback-based coupling is a crucial component of depth and egomotion estimation that promotes scale-consistency between depth and egomotion, which significantly boosts the overall system accuracy and improves generalization. In addition to feedback coupling, we incorporate indirect coupling into our system using an inference-time PFT strategy to achieve *tight coupling* of predictions; that is, our approach links depth to egomotion, and vice versa, such that an improvement in one directly leads to an improvement in the other.

### 3 Approach

We detail our tightly-coupled approach in three parts. First, we introduce the baseline (decoupled) depth and egomotion networks, and the self-supervised loss formulation used to train them. Second, we introduce feedback coupling based on iterative view synthesis. Finally, we present our inference-time depth optimization framework that forms the final component of our tightly-coupled framework for estimating depth and egomotion. See Figure 2 for an illustration of our system.

#### 3.1 Baseline depth and egomotion framework

For a single image pair consisting of a source and target image,  $\mathbf{x} = \{\mathbf{I}_s, \mathbf{I}_t\}$ , the latent variables of interest are the target image depth  $\mathbf{D}_t \in \mathbb{R}^{H \times W}$ , and the inter-frame pose change (egomotion)  $\mathbf{T}_{st} \in \text{SE}(3)$  between the images. We produce these estimates from two separate networks:  $\mathbf{D}_t = f_{\theta_D}(\mathbf{I}_t)$ ,  $\mathbf{T}_{st} = f_{\theta_E}(\mathbf{I}_s, \mathbf{I}_t)$ , which are jointly trained by minimizing a photometric reconstruction loss that compares a reconstructed target image  $\mathbf{I}'_s$  with the observed target image:

$$\mathcal{L}_{photo} = (1 - \alpha) |\mathbf{I}'_s - \mathbf{I}_t| + \alpha \mathcal{L}_{SSIM}(\mathbf{I}'_s, \mathbf{I}_t), \quad (1)$$

which is a weighted combination of the  $L_1$  loss and a structural similarity (SSIM) loss [43]. A spatial transformer [18] is used to reconstruct  $\mathbf{I}'_s$  from  $\mathbf{I}_s$  by populating each target image pixel coordinate  $\mathbf{u}'$  with the value from its corresponding location in the source image:

$$\mathbf{I}'_s(\mathbf{u}') = \mathbf{I}_s(\mathbf{u}), \quad \mathbf{u} = \pi(\mathbf{T}_{st}\pi^{-1}(\mathbf{u}')), \quad (2)$$

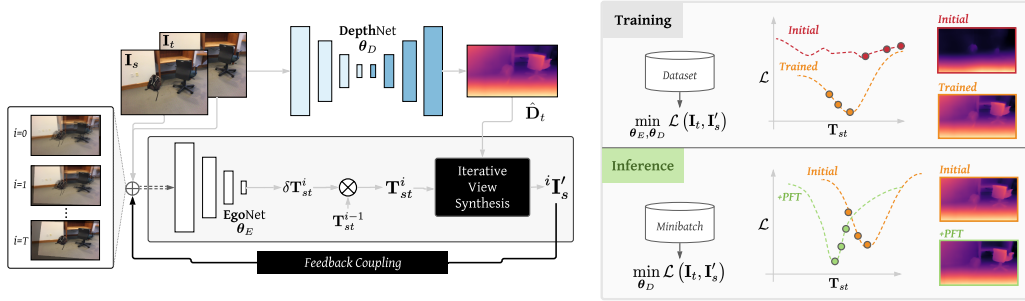


Figure 2: System overview. We use feedback coupling through iterative view synthesis [28] to produce an egomotion prediction that is notably a function of depth. At inference time, the depth network weights are updated via gradient descent to further minimize the sample-wise loss, and as a result of our unique coupling scheme, both depth and egomotion are improved.

where a pinhole camera projection model  $\pi(\mathbf{p}) = \mathbf{K}_z^{-1} \mathbf{u}$  relates a 3D point in the scene to its 2D image coordinate, and its inverse  $\mathbf{p} = \pi^{-1}(\mathbf{u})$  does the opposite, using the estimated per-pixel depth  $z$ . We additionally include two regularization losses to encourage the depth network to produce a realistic representation of the scene: a smoothness loss  $\mathcal{L}_{smooth}$  [12], and the geometric consistency loss  $\mathcal{L}_{GC}$  [3]. Our total *per-sample* loss is:

$$\mathcal{L} = \lambda_{photo} \mathcal{L}_{photo}(\mathbf{I}'_s, \mathbf{I}_t) + \lambda_{smooth} \mathcal{L}_{smooth}(\mathbf{I}_t, \mathbf{D}_t) + \lambda_{GC} \mathcal{L}_{GC}(\mathbf{D}_t, \mathbf{D}_s, \mathbf{T}_{st}). \quad (3)$$

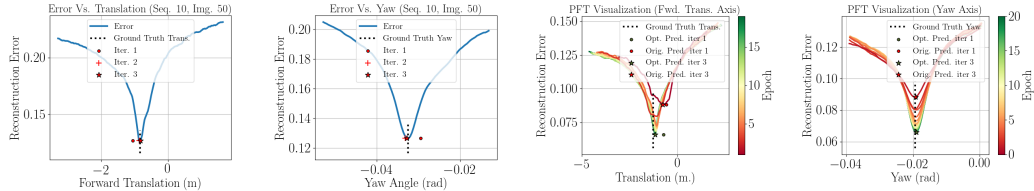
This baseline system employs no coupling aside from the indirect coupling that happens during training. To better couple our predictions, we next describe our feedback coupling approach that relies on iterative view synthesis.

### 3.2 Feedback-coupled egomotion prediction through iterative view synthesis

In the spirit of [28], we extend the standard egomotion estimation approach to incorporate feedback through iterative view synthesis. We perform multiple forward passes through the network and reformulate the egomotion network input as a photometric cost map that is updated after each iteration. Our network structure remains the same as the baseline network from Section 3.1; the only difference is that multiple passes through the network are made, where the  $i^{\text{th}}$  pass takes as input a recursively-updated cost map based on the images  $\{^i \mathbf{I}'_s, \mathbf{I}_t\}$ . Each pass through the network produces a correction  $\delta \xi_{s't}^i = f_{\theta_E}({}^i \mathbf{I}'_s, \mathbf{I}_t)$  that further aligns the current reconstructed source image  ${}^i \mathbf{I}'_s$  with the target image. Each correction is compounded together to produce the full pose change between the original source and target image:

$$\mathbf{T}_{st} = \left( \prod_{i=1}^T \delta \mathbf{T}_{s't}^i \right) \mathbf{T}_{st}^0 \approx \text{Exp} \left( \sum_{i=1}^T \delta \xi_{s't}^i \right) \mathbf{T}_{st}^0, \quad (4)$$

where in practice we parameterize our correction as an unconstrained vector from the  $\mathfrak{se}(3)$  Lie algebra,  $\delta \xi_{s't}^i \in \mathbb{R}^6$ , and then apply the exponential map [2] to produce an on-manifold  $\text{SE}(3)$  correction. We view the first pass through the network to be a correction to an *a priori* null egomotion initialization  $\mathbf{T}_{st}^0$  that attempts to align the original source image with the target image. In subsequent iterations, the warped image and the target image are used as input to produce an egomotion correction that further aligns the input image pair; notably, since  ${}^i \mathbf{I}'_s$  is a function of the current depth and egomotion predictions, these corrections can take into account the error that is explicitly encoded into the input cost map that cause the input images to be misaligned. Importantly, scale inconsistency between the network predictions can be accounted for in subsequent iterations. To demonstrate the impact of incorporating iteration, we visualize some sample-specific photometric reconstruction loss curves (as a function of egomotion) in Figure 3a (see the supplementary material for a description of how these curves were generated). Here, we observe that the egomotion predictions iteratively converge to the minimum loss. Figure 5b illustrates how applying more iterations improves convergence and generalization during training.



(a) Feedback-based coupling iteratively updates the ego- (b) Incorporating indirect coupling through PFT reduces the overall loss by improving depth accuracy.

Figure 3: 1D loss experiments illustrating the impact of adding coupling at inference time.

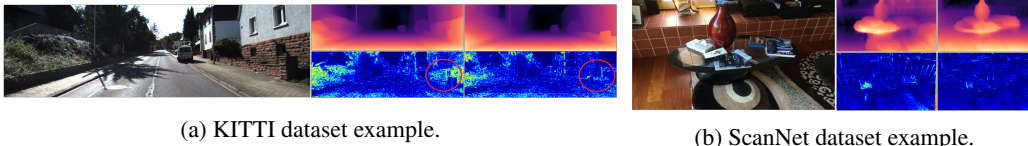


Figure 4: Depth predictions and reconstruction errors before (middle) and after (right) our inference-time depth optimization.

### 3.3 Tightly-coupled depth and egomotion optimization

Having coupled depth with egomotion to via iterative view synthesis, the natural extension is to then do the converse: couple egomotion with the depth. Although incorporating such two-way coupling (as done in DRO) is an appealing solution, we note an important drawback to this approach. Namely, modifications must be made to the training procedure in order to maintain stability during training, which may additionally lead to instability at inference time and therefore limit the use of online weight refinement. To avoid this, we instead incorporate an inference-time PFT strategy to refine the depth network weights. Namely, we use the Adam [19] optimizer to refine the depth network weights to further minimize a self-supervised loss. Notably, by incorporating our feedback-coupled egomotion network with our depth optimizer, we can achieve *tightly-coupled* optimization of depth and egomotion. The key to our optimization procedure is that our egomotion network’s predictions are *a function of depth*: as the depth predictions are refined, we recompute the egomotion prediction via our egomotion network, which has been trained to minimize the reconstruction loss given the current depth prediction. Effectively, this allows us to produce refined depth *and* egomotion predictions through optimization of our depth network only.

To perform PFT at inference time, we minimize the same loss as the one defined in Equation (3) but replace the smoothness term in with a depth prior that ensures the optimized depth  $\mathbf{D}_t^*$  remains similar to the original depth prediction:  $\mathcal{L}_{prior} = \mathcal{L}_{SSIM}(\mathbf{D}_t^*, \mathbf{D}_t)$ . Figure 3b illustrates our tightly-coupled optimization procedure in one dimension for a single inference-time sample. Beginning with the initial (red) loss curve produced by our trained depth network, the egomotion network recursively updates its predictions to converge to the (suboptimal) minimum. Each epoch of the inference-time depth optimizer shifts the loss to a new (lower) minimum by improving the quality of the depth prediction; then, given this new depth prediction, our egomotion network is able to converge to the new minima. We visualize an example of the improvement in depth accuracy (and the corresponding reduction in the photometric reconstruction error) this approach produces in Figure 4.

## 4 Experiments & results

To elucidate and validate our approach, we provide details of our network structure and training procedure, and follow this with extensive experimental validation on the KITTI, ScanNet, and Oxford RobotCar datasets. Specifically, we evaluate the performance of our tightly-coupled system on depth and egomotion benchmarks from KITTI and ScanNet, showing that we achieve state-of-the-art accuracy on the KITTI odometry benchmarks in addition to the ScanNet benchmarks. Further, we include ablation studies that indicate how both feedback and indirect coupling, although both useful on their own, complement each other when combined. Finally, we include demonstrate some additional benefits of feedback coupling; in particular, this added coupling improves generalization

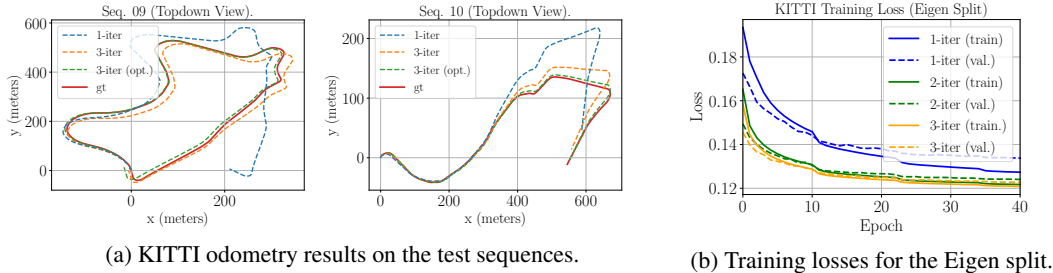


Figure 5: Results for the KITTI dataset.

across datasets, which we demonstrate through cross-dataset evaluation (from KITTI to Oxford RobotCar). For further information, we also refer the reader to the supplementary material.

**Datasets** We evaluate our system on outdoor and indoor datasets. The KITTI dataset [10, 11] is an outdoor driving dataset commonly used for evaluating depth and egomotion. For depth evaluation, we follow the Eigen train/test split [8]. For odometry evaluation, we train with sequences 00, 02, 05–08, and test on sequences 09–10. Our networks take as input images downsized to  $192 \times 640$ . ScanNet [7] is a large indoor dataset with 2.5M views in 1513 sequences. We follow the training/test split from [35], where the first 1413 sequences are used for training, and 2000 image pairs from the remaining 100 sequences are selected for testing. Our networks use images downsized to  $256 \times 448$ .

**Evaluation metrics** To be consistent with existing literature, we evaluate our approach by computing the commonly-reported metrics for each respective dataset. For KITTI depth evaluation, we follow the standard procedure from [13] and report depth accuracy using per-image median ground truth scaling. For odometry evaluation, we report the average translational and rotational errors ( $t_{err}(\%)$ ,  $r_{err}(^\circ/100m)$ ) over possible sub-sequences of length (100, 200, ..., 800) meters. Prior to evaluating these odometry metrics, we align the (unscaled) trajectories with ground truth by applying a constant scale factor to the translation values of the estimated trajectory. For evaluation on ScanNet, we report the depth and camera pose metrics as described in [35], and similar to existing literature, use image-wise rescaling to align the predictions with ground truth for both depth and poses.

**Implementation details** We use the same depth and egomotion network structure from [39], implemented in PyTorch [29].<sup>3</sup> The depth network is a U-Net [32] encoder-decoder, consisting of a ResNet18 [17] encoder, and a decoder based on the networks from Monodepth2 [13] and DNet [47] (we modify Monodepth2 by adding “dense connected prediction” (DCP) layers from DNet). The egomotion network is a 7-layer CNN that takes as input a source-target image pair, and returns a 6D pose vector. For KITTI and ScanNet experiments, we pretrain our networks on images from the Oxford RobotCar dataset [25]. We train our models on an NVIDIA Titan V GPU for 25, 45, and 15 epochs on the KITTI (odometry and eigen splits) and ScanNet datasets respectively using the Adam optimizer [19] ( $\beta_1 = 0.9$ ,  $\beta_2 = 0.999$ ). We use a learning rate of  $(1 \times 10^{-4}, 2 \times 10^{-4})$  for the depth and egomotion network respectively, that is halved four times over the duration of training. During training we apply data augmentation in the form of horizontal flipping and modifications to hue, saturation, contrast, and brightness. For our training loss (Equation (3)), we use  $\alpha = 0.85$ ,  $\lambda_{photo} = 1$ ,  $\lambda_{smooth} = 0.05$ ,  $\lambda_{GC} = 0.15$ . Each sample consists of three consecutive images (the middle target image, and its two adjacent source images). We evaluate the loss only on the highest resolution image scale, rather than using a multiscale approach. To introduce additional motion, the loss is evaluated in both the forward and inverse directions (in the inverse direction,  $\mathbf{I}_t$  is used to reconstruct  $\mathbf{I}_s$ ). We use the “automasking”, “minimum reprojection” techniques from [13], in addition to the self-discovered mask from [3] to ignore/downweight unreliable pixels in our loss.

**Some notes on PFT** Our PFT optimization scheme uses the Adam optimizer to update the depth network weights, while the egomotion network weights are fixed. Following [27], we only update the depth encoder weights instead of updating the full depth network. We use the same hyperparameters

<sup>3</sup>available at [https://github.com/utiasSTARS/learned\\_scale\\_recovery](https://github.com/utiasSTARS/learned_scale_recovery).

Method		Depth ↓				Pose ↓			
		Abs Rel	Sq Rel	RMSE	RMSE log	SI Inv	Rot (deg)	Tr (deg)	Tr (cm)
	LSD-SLAM [9]	0.268	0.427	0.788	0.330	0.323	4.409	34.36	21.40
Sup.	DeMon [37]	0.231	0.520	0.761	0.289	0.284	3.791	31.626	15.50
	BANet [35]	0.161	0.092	0.346	0.214	0.184	1.018	20.577	3.39
	DeepSFM [45]	0.227	0.170	0.479	0.271	0.268	1.588	30.613	—
	DeepV2D [36]	0.069	0.018	0.196	0.099	0.097	0.692	11.731	1.902
	Luo et al. <sup>1</sup> [24]	0.073	0.037	0.217	0.105	0.103	—	—	—
	DRO [14]	<b>0.053</b>	<b>0.017</b>	<b>0.168</b>	<b>0.081</b>	<b>0.079</b>	<b>0.473</b>	<b>9.219</b>	<b>1.160</b>
Self-Sup.	DRO [14]	0.140	0.127	0.496	0.212	0.210	0.691	11.702	1.647
	Ours (4/8 iter.)	<b>0.088</b>	<b>0.038</b>	<b>0.260</b>	<b>0.125</b>	<b>0.122</b>	<b>0.547</b>	<b>10.482</b>	<b>1.290</b>
	Ours (using GT Depth)	—	—	—	—	—	0.516	10.366	1.247
Ablation	1/1 iter. (no PFT)	0.181	0.117	0.462	0.229	0.223	1.948	43.363	5.612
	1/1 iter.	0.186	0.125	0.462	0.233	0.228	1.948	43.363	5.612
	2/2 iter. (no PFT)	0.126	0.062	0.342	0.167	0.162	1.137	20.790	2.800
	2/4 iter. (no PFT)	0.126	0.062	0.342	0.167	0.162	0.958	17.496	2.270
	2/4 iter.	0.111	0.054	0.302	0.150	0.147	0.821	15.195	1.952
	4/4 iter.	0.092	0.040	0.266	0.129	0.126	0.695	12.340	1.669
	4/8 iter. (no PFT)	0.103	0.044	0.292	0.140	0.137	0.690	12.389	1.635

<sup>1</sup> This method is self-supervised but it retrains the supervised model from [31] on ScanNet.

Table 2: ScanNet results for the standard two-view test set split. The ablation study indicates that more iterations and applying PFT at inference time leads to improved performance. For our methods we specify the number of iterations applied during training ( $x$ ) and inference ( $y$ ) as  $x/y$  iter.

that were used during training, and minimize the same loss function while replacing the depth smoothness loss with the depth prior loss ( $\lambda_{prior} = 0.1$ ). For every test set sample, 20 optimization “epochs” are performed. We perform the optimization over a minibatch, which helps with regularization and leverages available GPU memory to increase the optimization speed. Instead of returning the network predictions from the final epoch, we average the predictions from the last 5 epochs to prevent a noisy gradient step from negatively impacting the optimization. Lastly, in the course of evaluating our approach on the KITTI odometry dataset, we identified that sample-wise optimization often increases *inter-frame* scale drift, since the PFT procedure can independently shift the scale factor for individual samples within the test sequences. To promote a uniform scale factor across an entire sequence, we incorporate the (self-supervised) online scale recovery module based on DNet [47]; for each image, we estimate the camera height (relative to the ground plane) using our depth prediction, and then normalize the corresponding translation prediction using this quantity. We refer the reader to Table 5 for ablation experiments that present the accuracy of our method without applying this rescaling. It is important to note that this type of scale inconsistency differs from the *inter-network* scale inconsistency that we addressed in this work through the introduction of tightly-coupled networks.

#### 4.1 Evaluation on ScanNet and KITTI

**ScanNet results** Table 2 presents our results on the ScanNet test split. Our method significantly outperforms the self-supervised variant of DRO, and is competitive with supervised methods. We additionally include the pose results of our egomotion network when using the available ground truth depth (instead of our predicted depth) to iteratively warp the source image. The improved pose accuracy indicates that our egomotion network is able to function with an arbitrary depth map that was not present during training. Our ablation study reveals that feedback coupling (through iteration) is crucial for improving accuracy; without this, even the PFT has very little impact.

**KITTI results** Table 3 and Figure 5a evaluates our tightly-coupled system on the KITTI odometry test sequences, which shows that our proposed method achieves state-of-the-art egomotion accuracy compared with other learning-based methods. Our Table 5 ablation study indicates that coupling is crucial for achieving this level of accuracy; including feedback and applying our PFT strategy are both highly effective, but incorporating both leads to the best performance. We note that our coupling approach (with or without PFT) produces better egomotion accuracy than more simplistic direct coupling methods [1, 42] that treat depth as an input into the egomotion network.

Method	Seq. 09		Seq. 10	
	$t_{err}$ (%)	$r_{err}$ (°/100m)	$t_{err}$ (%)	$r_{err}$ (°/100m)
SfMLearner [50]	11.32	4.07	15.25	4.06
SC-SfMLearner [3]	8.24	2.19	10.7	4.58
Ambrus et al. [1]	6.72	1.69	9.52	1.59
ManyDepth <sup>1</sup> [44]	13.36	2.93	10.18	4.25
Li et al. [23]	5.89	3.34	4.79	0.83
Wang et al. [42]	9.30	3.50	7.21	3.90
<b>DOC [49]</b>	2.02	0.61	2.29	1.10
<b>Shu et al. [34]</b>	8.75	2.11	10.67	4.91
<b>Ours (4-iter)</b>	<b>1.19</b>	<b>0.30</b>	<b>1.34</b>	<b>0.37</b>

<sup>1</sup> Based on their publicly available model (trained on the Eigen split), without test-time PFT.

Table 3: KITTI odometry results on the standard test sequences. Methods with test-time PFT are in **bold**.

Table 6 evaluates our system’s depth accuracy on the Eigen test split; notably, we are competitive with other monocular, self-supervised methods, but lag behind some recent approaches like ManyDepth [44]. We emphasize the utility of our method producing accurate depth *and* egomotion, whereas ManyDepth and Shu et al. [34] are only able to estimate depth with a high degree of accuracy.

**Feedback coupling experiments** Lastly, we present evidence that supports the utility of using feedback for egomotion estimation. First, we evaluate how feedback through iteration improves generalization to unseen data. We demonstrate this by evaluating our network on image pairs with inter-frame perspective changes that are significantly larger than those within the dataset (which can occur due to increased camera velocity or decreased camera framerate). To do so, we modify the KITTI data by skipping images (i.e., adopting a stride greater than one), and we evaluate test sequence odometry error as a function of increased perspective change. Detailed in Figure 6a, we see that as the number of iterations increases, the generalization performance improves. Second, we include a cross-dataset evaluation that tests our KITTI-trained model on the Oxford RobotCar dataset [25]. Table 4 depicts these results, which indicate that iteration is crucial for generalizing to unseen data.

Next, we verify how *robust* the feedback coupling mechanism is by demonstrating its ability to minimize error in the face of large perturbations being applied to the initial egomotion prediction. To investigate this, we apply perturbations (in the forward translation direction, and along the yaw axis) to all of the egomotion predictions within our KITTI test sequences, and then evaluate the overall odometry error. We repeat this experiment with increasing perturbation ranges, and summarize the results in Figure 6b. Here, we see that the increase in error from adding perturbations is completely mitigated by applying only two extra iterations. During these subsequent iterations, the network, which takes as input the (erroneously) warped source image, produces *corrections* that effectively account for the initial perturbation.

Finally, we verify our Section 3.2 claim that appropriate coupling of the network predictions improves inter-network scale consistency. To do so, we rescale all of the depth predictions for the KITTI

Training Dataset	Subseq. 0		Subseq. 1	
	$t_{err}$ (%)	$r_{err}$ (°/100m)	$t_{err}$ (%)	$r_{err}$ (°/100m)
Ox. (1-iter)	7.75	3.26	9.50	3.43
KITTI (1-iter)	36.45	12.05	32.99	13.81
Rel. Change	-370.32%	-269.63%	-247.26%	-302.62%
Ox. (3-iter)	4.84	2.18	6.46	2.38
KITTI (3-iter)	5.83	3.11	11.44	4.54
Rel. change	-20.45%	-42.66%	-77.09%	-90.76%

Table 4: Cross-dataset evaluation results on sequences from 2014-11-18-13-20-12. When training on KITTI and testing on Oxford, the 3-iteration model generalizes significantly better than the 1-iteration model.

# Egomotion Iter. (train/test)	PFT Params	Seq. 09		Seq. 10	
		$t_{err}$ (%)	$r_{err}$ (°/100m)	$t_{err}$ (%)	$r_{err}$ (°/100m)
1 / 1	—	8.42	2.52	9.10	4.11
1 / 3	—	6.16	1.51	10.13	2.74
2 / 2	—	4.49	1.22	6.86	2.09
4 / 4	—	2.98	0.66	3.38	1.02
4 / 6	—	3.02	0.69	3.03	10.93
1 / 1	$\theta_D + \theta_E$	2.00	0.51	2.36	0.95
4 / 4	$\theta_D$	1.19	0.30	1.34	0.37
4 / 4 (no DNet scaling)	$\theta_D$	2.36	0.30	2.36	0.38
4 / 4 (no $\mathcal{L}_{prior}$ )	$\theta_D$	1.79	0.275	2.13	0.46
4 / 4	$\theta_D + \theta_E$	1.28	0.31	1.36	0.35

Table 5: Ablation study showing the effect of feedback coupling and indirect coupling (through PFT) at inference time. Including both leads to the lowest error.

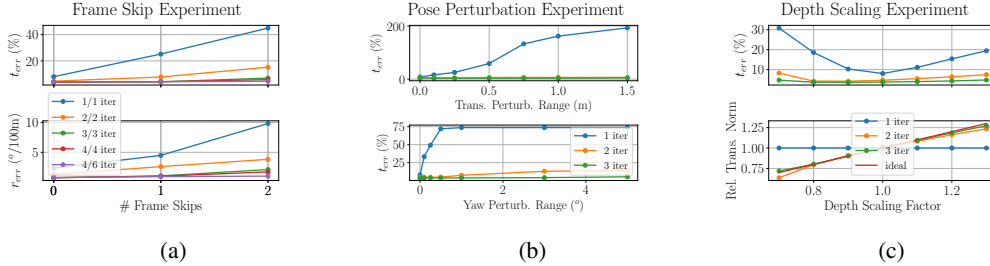


Figure 6: Summarizing the experiments that demonstrate the utility of using an iterative egomotion network.

Method	Test-Time PFT	Error ↓				Accuracy ↑		
		Abs Rel	Sq Rel	RMSE	RMSE log	$\delta < 1.25$	$\delta < 1.25^2$	$\delta < 1.25^3$
SC-SfMLearner [3]		0.128	1.047	5.234	0.208	0.846	0.947	0.976
Nabavi et al. [28]		0.160	1.195	5.916	0.245	0.774	0.917	0.964
MonoDepth2 [13]		0.115	0.903	4.863	0.193	0.877	0.959	0.981
PackNet-SfM [15]		0.107	0.803	4.566	0.197	0.876	0.957	0.980
Guizilini et al. [16]		0.111	0.785	4.601	0.189	0.878	—	—
DRO [14]		<b>0.088</b>	0.797	4.464	0.212	0.899	0.959	0.980
GLNet [5]	✓	0.099	0.796	4.743	0.186	0.884	0.955	0.979
ManyDepth [44]	✓	0.090	0.713	4.261	<b>0.170</b>	0.914	<b>0.966</b>	<b>0.983</b>
Luo et al. [24]	✓	0.130	2.086	4.876	0.205	0.878	0.946	0.970
McCraith et al. [27]	✓	<b>0.089</b>	0.747	4.275	0.173	0.912	0.964	0.982
Shu et al. [34]	✓	<b>0.088</b>	<b>0.712</b>	<b>4.137</b>	0.169	<b>0.915</b>	0.965	0.982
CoMoDA [20]	✓	0.102	0.871	4.596	0.183	0.898	0.961	0.981
Ours	✓	0.097	0.791	4.383	0.178	0.896	0.961	0.982

Table 6: Monocular depth prediction results for self-supervised methods on the Eigen test split [8]. We report results from our depth network following inference time PFT (paired with a 4-iteration egomotion network). In all other cases, we report the results from the image resolution closest to ours.

test sequences by a constant scale factor, and then observe how the egomotion scale factor (i.e., the translation norm) changes in response to the modified depth predictions. Figure 6c illustrates that the average change in the translation norms (for the iterative models) are proportional to the applied depth scaling factor. This provides support for the notion that the egomotion network is able to infer scale from depth predictions via our feedback coupling strategy.

**Limitations** Though our PFT strategy improves overall depth accuracy, it is unable to accurately handle dynamic objects; this is one of the primary reasons why our method is less accurate on the KITTI depth evaluation. Further, our test-time PFT strategy, whose runtime is on the order of 3 FPS, is computationally inefficient compared to decoupled methods that do not update network weights at inference time. We note that this is an ongoing challenge for PFT methods that is actively being addressed [27]. We aim to resolve these issues in future work.

## 5 Conclusion

In this paper, we demonstrated that an appropriate *coupling* of depth and egomotion networks improves performance in self-supervised SfM. We introduced a taxonomy of coupling methods, and discussed the potential benefits of incorporating each to promote consistency between depth and egomotion predictions at training and inference time. We noted the particular importance of feedback coupling as a method to iteratively update an initial prediction to further minimize the loss. Building on these insights, we presented our own *tightly-coupled* approach and, through extensive experiments, showed that our system was consistently accurate across indoor and outdoor datasets and achieved state-of-the-art accuracy on several key benchmarks. In future work, we aim to generalize our tightly-coupled framework to incorporate additional sensor modalities such as inertial measurement units.

## Broader Impact

Our contribution is a perception module that builds a representation of 3D geometry by learning to predict scene depth and camera motion from video. Such a system could be incorporated into robotic and autonomous systems (such as self-driving vehicles). Overall, this contribution can impact the level of autonomy in these vehicles, as full autonomy requires a high degree of scene understanding. Through autonomy, many opportunities will arise to improve the overall quality of life for many people; however, this comes with the risk of worker displacement in manufacturing, transportation, and other industries.

Like most learning-based perception systems, there are safety concerns when these systems are deployed on robotic platforms, as failure can lead to loss of life. Our system should never be used without having redundancies and safety checks in place. We, however, address some safety concerns by employing self-supervised loss functions that can be used to continually retrain our system with incoming data. This allows our system to specifically account for changes to the environment over time, or to adapt as the robot traverses to a new environment.

## Acknowledgments and Disclosure of Funding

This research was supported in part by the Canada Research Chairs program. We gratefully acknowledge the contribution of NVIDIA Corporation, who provided the Titan X GPU used for this research through their Hardware Grant Program.

## References

- [1] R. Ambrus, V. Guizilini, J. Li, S. Pillai, and A. Gaidon. Two stream networks for self-supervised ego-motion estimation. In Conf. Robot Learning (CoRL), pages 1052–1061, 2020.
- [2] T. Barfoot. State Estimation for Robotics. Cambridge University Press, New York, NY, USA, 1st edition, 2017. ISBN 1107159393, 9781107159396.
- [3] J. Bian, Z. Li, N. Wang, H. Zhan, C. Shen, M. Cheng, and I. Reid. Unsupervised scale-consistent depth and ego-motion learning from monocular video. In Proc. Conf. Neural Inf. Process. Syst. (NeurIPS), pages 35–45, 2019.
- [4] V. Casser, S. Pirk, R. Mahjourian, and A. Angelova. Unsupervised monocular depth and ego-motion learning with structure and semantics. In Proc. IEEE Conf. Comput. Vision Pattern Recognition (CVPR) Workshops, 2019.
- [5] Y. Chen, C. Schmid, and C. Sminchisescu. Self-supervised learning with geometric constraints in monocular video: Connecting flow, depth, and camera. In Proc. IEEE/CVF Int. Conf. Comput. Vision (ICCV), pages 7063–7072, 2019.
- [6] R. Clark, M. Bloesch, J. Czarnowski, S. Leutenegger, and A. Davison. Learning to solve nonlinear least squares for monocular stereo. In Proc. Eur. Conf. Comput. Vision (ECCV), pages 284–299, 2018.
- [7] A. Dai, A. Chang, M. Savva, M. Halber, T. Funkhouser, and M. Nießner. Scannet: Richly-annotated 3d reconstructions of indoor scenes. In Proc. IEEE Conf. Comput. Vision Pattern Recognition (CVPR), pages 5828–5839, 2017.
- [8] D. Eigen and R. Fergus. Predicting depth, surface normals and semantic labels with a common multi-scale convolutional architecture. In Proc. IEEE Conf. Comput. Vision (ICCV), pages 2650–2658, 2015.
- [9] J. Engel, T. Schöps, and D. Cremers. Lsd-slam: Large-scale direct monocular slam. In Proc. Eur. Conf. Comput. Vision (ECCV), pages 834–849. Springer, 2014.
- [10] A. Geiger, P. Lenz, and R. Urtasun. Are we ready for autonomous driving? the KITTI vision benchmark suite. In Proc. IEEE Conf. Comput. Vision Pattern Recognition (CVPR), pages 3354–3361, 2012.

- [11] A. Geiger, P. Lenz, C. Stiller, and R. Urtasun. Vision meets robotics: The KITTI dataset. Int. J. Robot. Res. (IJRR), 32(11):1231–1237, 2013.
- [12] C. Godard, O. Aodha, and G. Brostow. Unsupervised monocular depth estimation with left-right consistency. In Proc. IEEE Conf. Comput. Vision Pattern Recognition (CVPR), pages 270–279, 2017.
- [13] C. Godard, O. Aodha, M. Firman, and G. Brostow. Digging into self-supervised monocular depth estimation. In Proc. IEEE Conf. Comput. Vision Pattern Recognition (CVPR), pages 3828–3838, 2019.
- [14] X. Gu, W. Yuan, Z. Dai, S. Zhu, C. Tang, and P. Tan. Dro: Deep recurrent optimizer for structure-from-motion. arXiv preprint arXiv:2103.13201, 2021.
- [15] V. Guizilini, R. Ambrus, S. Pillai, A. Raventos, and A. Gaidon. 3d packing for self-supervised monocular depth estimation. In Proc. IEEE/CVF Conf. Comput. Vision Pattern Recognition (CVPR), pages 2485–2494, 2020.
- [16] V. Guizilini, L. Vitor, A. Jie, R. Ambrus, S. Pillai, and A. Gaidon. Robust semi-supervised monocular depth estimation with reprojected distances. In Conf. Robot Learning (CoRL), pages 503–512, 2020.
- [17] K. He, X. Zhang, S. Ren, and J. Sun. Deep residual learning for image recognition. In Proc. IEEE Conf. Comput. Vision Pattern Recognition (CVPR), pages 770–778, 2016.
- [18] M. Jaderberg, K. Simonyan, A. Zisserman, and K. Kavukcuoglu. Spatial transformer networks. In Proc. Conf. Neural Inf. Process. Syst. (NeurIPS), pages 2017–2025, 2015.
- [19] D. P. Kingma and J. Ba. Adam: A method for stochastic optimization. arXiv preprint arXiv:1412.6980, 2014.
- [20] Y. Kuznetsov, M. Proesmans, and L. V. Gool. Comoda: Continuous monocular depth adaptation using past experiences. In Proc. IEEE Winter Conf. Appl. Comput. Vision (WACV), pages 2907–2917, 2021.
- [21] H. Li, A. Gordon, H. Zhao, V. Casser, and A. Angelova. Unsupervised monocular depth learning in dynamic scenes. arXiv preprint arXiv:2010.16404, 2020.
- [22] R. Li, S. Wang, Z. Long, and D. Gu. UnDeepVO: Monocular visual odometry through unsupervised deep learning. In Proc. IEEE Int. Conf. Robot. Autom. (ICRA), pages 7286–7291, 2018. doi: 10.1109/ICRA.2018.8461251.
- [23] S. Li, X. Wang, Y. Cao, F. Xue, Z. Yan, and H. Zha. Self-supervised deep visual odometry with online adaptation. In Proc. IEEE Conf. Comput. Vision Pattern Recognition (CVPR), pages 6339–6348, 2020.
- [24] X. Luo, J. Huang, R. Szeliski, K. Matzen, and J. Kopf. Consistent video depth estimation. ACM Trans. Graphics (TOG), 39(4):71–1, 2020.
- [25] W. Maddern, G. Pascoe, C. Linegar, and P. Newman. 1 Year, 1000km: The Oxford RobotCar Dataset. Int. J. Robot. Res. (IJRR), 36(1):3–15, 2017. doi: 10.1177/0278364916679498.
- [26] R. Mahjourian, M. Wicke, and A. Angelova. Unsupervised learning of depth and ego-motion from monocular video using 3d geometric constraints. In Proc. IEEE Conf. Comput. Vision Pattern Recognition (CVPR), pages 5667–5675, 2018.
- [27] R. McCraith, L. Neumann, A. Zisserman, and A. Vedaldi. Monocular depth estimation with self-supervised instance adaptation. arXiv preprint arXiv:2004.05821, 2020.
- [28] S. Nabavi, M. Hosseinzadeh, R. Fahimi, and Y. Wang. Unsupervised learning of camera pose with compositional re-estimation. In Proc. IEEE/CVF Winter Conf. Appl. Comput. Vision, pages 11–20, 2020.

- [29] A. Paszke, S. Gross, S. Chintala, G. Chanan, E. Yang, Z. DeVito, Z. Lin, A. Desmaison, L. Antiga, and A. Lerer. Automatic differentiation in PyTorch. In Workshop on Automatic Differentiation, Conf. Neural Inf. Process. Syst. (NeurIPS), 2017.
- [30] S. Qiao, H. Wang, C. Liu, W. Shen, and A. Yuille. Micro-batch training with batch-channel normalization and weight standardization. arXiv preprint arXiv:1903.10520, 2019.
- [31] R. Ranftl, K. Lasinger, D. Hafner, K. Schindler, and V. Koltun. Towards robust monocular depth estimation: mixing datasets for zero-shot cross-dataset transfer. IEEE Trans. Pattern Anal. Machine Intell., 2020.
- [32] Ronneberger, O. and Fischer, P. and Brox, T. U-Net: Convolutional networks for biomedical image segmentation. In Proc. Int. Conf. Medical Image Computing Computer-Assisted Intervention, pages 234–241. Springer, 2015.
- [33] T. Shen, Z. Luo, L. Zhou, H. Deng, R. Zhang, T. Fang, and L. Quan. Beyond photometric loss for self-supervised ego-motion estimation. In Proc. IEEE Int. Conf. Robot. Autom. (ICRA), pages 6359–6365. IEEE, 2019.
- [34] C. Shu, K. Yu, Z. Duan, and K. Yang. Feature-metric loss for self-supervised learning of depth and egomotion. In Proc. Eur. Conf. Comput. Vision (ECCV), pages 572–588. Springer, 2020.
- [35] C. Tang and P. Tan. Ba-net: Dense bundle adjustment network. arXiv preprint arXiv:1806.04807, 2018.
- [36] Z. Teed and J. Deng. Deepv2d: Video to depth with differentiable structure from motion. In Conf. Learning Representations (ICLR), 2020.
- [37] B. Ummenhofer, H. Zhou, J. Uhrig, N. Mayer, E. Ilg, A. Dosovitskiy, and T. Brox. Demon: Depth and motion network for learning monocular stereo. In Proc. IEEE Conf. Comput. Vision Pattern Recognition (CVPR), pages 5038–5047, 2017.
- [38] S. Vijayanarasimhan, S. Ricco, C. Schmid, R. Sukthankar, and K. Fragkiadaki. SfM-Net: Learning of structure and motion from video. arXiv preprint arXiv:1704.07804, 2017.
- [39] B. Wagstaff and J. Kelly. Self-supervised scale recovery for monocular depth and egomotion estimation. arXiv preprint arXiv:2009.03787, 2020.
- [40] B. Wagstaff, V. Peretroukhin, and J. Kelly. Self-supervised deep pose corrections for robust visual odometry. In Proc. IEEE Int. Conf. Robot. Autom. (ICRA), pages 2331–2337. IEEE, 2020.
- [41] J. Wang, G. Zhang, Z. Wu, X. Li, and L. Liu. Self-supervised joint learning framework of depth estimation via implicit cues. arXiv preprint arXiv:2006.09876, 2020.
- [42] R. Wang, S. Pizer, and J. Frahm. Recurrent neural network for (un-) supervised learning of monocular video visual odometry and depth. In Proc. IEEE Conf. Comput. Vision Pattern Recognition (CVPR), pages 5555–5564, 2019.
- [43] Z. Wang, A. Bovik, H. Sheikh, and E. Simoncelli. Image quality assessment: from error visibility to structural similarity. IEEE Trans. Image Process., 13(4):600–612, 2004.
- [44] J. Watson, O. Aodha, V. Prisacariu, G. Brostow, and M. Firman. The temporal opportunist: Self-supervised multi-frame monocular depth. arXiv preprint arXiv:2104.14540, 2021.
- [45] X. Wei, Y. Zhang, Z. Li, Y. Fu, and X. Xue. Deepsfm: Structure from motion via deep bundle adjustment. In Proc. Eur. Conf. Comput. Vision (ECCV), pages 230–247. Springer, 2020.
- [46] Y. Wu and K. He. Group normalization. In Proc. Eur. Conf. Comput. Vision (ECCV), pages 3–19, 2018.
- [47] F. Xue, G. Zhuo, Z. Huang, W. Fu, Z. Wu, and M. A. Jr. Toward hierarchical self-supervised monocular absolute depth estimation for autonomous driving applications. arXiv preprint arXiv:2004.05560, 2020.

- [48] H. Zhan, R. Garg, C. Weerasekera, K. Li, H. Agarwal, and I. Reid. Unsupervised learning of monocular depth estimation and visual odometry with deep feature reconstruction. In Proc. IEEE Conf. Comput. Vision Pattern Recognition (CVPR), pages 340–349, 2018.
- [49] J. Zhang, W. Sui, X. Wang, W. Meng, H. Zhu, and Q. Zhang. Deep online correction for monocular visual odometry. arXiv preprint arXiv:2103.10029, 2021.
- [50] T. Zhou, M. Brown, N. Snavely, and D. Lowe. Unsupervised learning of depth and ego-motion from video. In Proc. IEEE Conf. Comput. Vision Pattern Recognition (CVPR), pages 1851–1858, 2017.
- [51] Y. Zou, P. Ji, Q. Tran, J. Huang, and M. Chandraker. Learning monocular visual odometry via self-supervised long-term modeling. arXiv preprint arXiv:2007.10983, 2020.

Table 7: The network layers for our egomotion network. **k** refers to the kernel size, **s** refers to the stride, **chns** refers to the input/output channels.

Egomotion Network					
Layer	k	s	chns	input	Activation
conv1	3	1	6/16	stacked-img-pair	WS+GN+ReLU
conv2	3	2	16/32	conv1	WS+GN+ReLU
conv3	3	3	32/64	conv2	WS+GN+ReLU
conv4	3	2	64/128	conv3	WS+GN+ReLU
conv5	3	2	128/256	conv4	WS+GN+ReLU
conv6	3	2	256/256	conv5	WS+GN+ReLU
conv7	3	2	256/256	conv6	WS+GN+ReLU
avgpool				conv7	-
poseconv	1	1	256/6	avgpool	-

## A Supplementary Material

### A.1 Network and training details

**Egomotion network** Table 7 describes the layers of the egomotion network that were used. Following each convolutional layer, weight standardization (WS) [30] and group normalization (GN) [46] are applied prior to the ReLU activation except the last, which must be able to produce unrestricted values.

**Depth network** Table 8 describes the layers of our depth network decoder, which is based on Monodepth2 [13]. Here, the output from the Resnet18 encoder (enc5) is upsampled, and passed through multiple convolution and upsampling layers, while being merged with additional skip connections (enc4, enc3, enc2). Rather than directly predicting the disparity (inverse depth) from these layers at multiple scales, we adopt the “dense connected prediction” (DCP) convolutional layers from DNet [47] to merge features from all of the resolution scales prior to regressing the inverse depth. Table 9 describes how the various layers from the depth decoder (i.e., iconv3, iconv2, iconv2) are passed into DCP convolution layers, which have sigmoid activations used to output disparity predictions whose values are within the range of [0, 1]. Note the final layer concatenates the dcp3, dcp2, dcp1 layer outputs to produce a multiscale disparity prediction.

The inverse depth output  $\mathbf{o}_t$  is then inverted, and constrained to be within the range  $[D_{min}, D_{max}]$ :

$$\mathbf{D}_t^{-1} = \frac{1}{D_{min}} + \left( \frac{1}{D_{max}} - \frac{1}{D_{min}} \right) \mathbf{o}_t.$$

For our experiments, we set these hyperparameters specifically for the dataset, and note that in the future this parameter can be learned [27]. We use [0.06, 2.67] for KITTI odometry, [0.1, 2.67] for KITTI Eigen, and [0.03, 3] for ScanNet.

**More training details** Our iterative egomotion network is trained with minimal applied changes to the baseline training procedure. To ensure stability, we only apply one iteration in the first epoch, and then increase to the specified number of iterations for the rest of the training. When training using multiple egomotion iterations, we only compute the loss once using the *final* egomotion prediction, rather than for the egomotion prediction after every iteration. This speeds up training, and allows the iterative approach to be easily incorporated into the standard self-supervised depth and egomotion pipeline. We note that multiple backpropagation steps (for every forward pass through the egomotion network) would better enforce accuracy across all iterations, rather than only enforcing accuracy for the final prediction, but was less feasible to implement. A simpler way to enforce accuracy across all iterations would be to randomize the number of egomotion iterations per minibatch.

**Oxford Robotcar pretraining** We initialize the depth and egomotion network weights via self-supervised training on the Oxford Robotcar dataset. Here, following the same training procedure (i.e., same loss function, same network structure, same hyperparameters), we train for 15

Table 8: The network layers for our depth decoder network. To merge the current layer with the ResNet18 layers, we upsampled (via nearest neighbour interpolation) them prior to applying the upconv convolution. Upsampling is indicated by  $\uparrow$ .

Depth Decoder					
Layer	k	s	chns	input	activation
upconv5	3	1	512/256	$\uparrow$ enc5	ELU
iconv5	3	1	256/256	upconv5	ELU
upconv4	3	1	256/128	$\uparrow$ iconv5	ELU
iconv4	3	1	128/128	upconv4 + enc4	ELU
upconv3	3	1	128/64	$\uparrow$ iconv4	ELU
iconv3	3	1	64/64	upconv3 + enc3	ELU
upconv2	3	1	64/64	$\uparrow$ iconv3	ELU
iconv2	3	1	64/64	upconv2 + enc2	ELU
upconv1	3	1	64/32	$\uparrow$ iconv2	ELU
iconv1	3	1	32/32	upconv1	ELU

Table 9: The DCP components of our decoder, that merge features from all scales to produce the disp1 (full resolution) prediction.

DCP Layers					
Layer	k	s	chns	input	activation
dcp3	3	1	64/8	iconv3	ELU
disp3	3	1	8/1	dcp3	sigmoid
dcp2	3	1	64/8	iconv2	ELU
disp2	3	1	16/1	$\uparrow$ dcp3, dcp2	sigmoid
dcp1	3	1	32/8	iconv1	ELU
disp1	3	1	24/1	dcp3, $\uparrow$ dcp2, $\uparrow$ dcp1	sigmoid

epochs on sequences 2014-11-18-13-20-12, 2015-07-08-13-37-17, 2015-07-10-10-01-59, 2015-08-12-15-04-18; we use the first and second subsequences of 2014-11-18-13-20-12 for validation and testing respectively. Note that this pretraining does not significantly affect our results, but simply ensures stability during training, as initializing from random weights is not always guaranteed to converge. Starting from an initialized model (that we can use for all of our KITTI and ScanNet experiments) simplifies our training scheme. We demonstrate that the added Oxford pretraining data does not result in a significant performance increase compared with solely using training data (see Table 10)

Method	Seq. 09		Seq. 10	
	$t_{err}$ (%)	$r_{err}$ ( $^{\circ}$ /100m)	$t_{err}$ (%)	$r_{err}$ ( $^{\circ}$ /100m)
Pretrained	1.19	0.30	1.34	0.37
No Pretraining	1.17	0.29	1.81	0.54

Table 10: Demonstrating the impact of using Oxford RobotCar pretraining for our KITTI odometry model. There is a small difference in the overall accuracy that comes from additionally using more data.

## A.2 Additional results

We include additional details and results for our experiments. First, we discuss how the 1D loss curves were generated, and provide additional examples of such curves. Then, we include more examples of predictions from our depth network. Next, we provide further details and results for our pose perturbation experiment, and for our depth scaling experiment. Finally, we include another ablation study for the KITTI depth results on the Eigen test split.

### A.2.1 Generation of 1D loss curves

For any source/target image pair, given a fixed target depth prediction, we visualize the photometric reconstruction loss surface by varying one of the six degrees of freedom of the egomotion prediction via a grid search. We demonstrate that the loss curve has a clear minimum that our egomotion network identifies by iteratively updating its prediction until the error is minimized. For image datasets generated with a forward facing camera on a ground vehicle (e.g., KITTI), there are two primary degrees of freedom: the forward translation (z-axis), and the yaw angle (about the y-axis). Thus, our experiments focus on these two degrees of freedom. To sample egomotion values, we generate the initial depth and egomotion predictions from our trained networks, and use a grid search to sample poses within a range centered around the initial prediction. For visualization purposes, we only vary a single degree of freedom of the egomotion at a time, while keeping the other values fixed with the initial prediction value. Note that we use DNet rescaling [47] to align the scale factor of the predictions with ground truth prior to generating these curves.

Concretely, one variable within the inter-frame pose prediction  $p_0 \in \{t_x, t_y, t_z, \theta_x, \theta_y, \theta_z\}$  is varied using a grid search to produce  $N$  values in the range  $[p_0 - y, p_0 + y]$ . For each value we compute the photometric reconstruction loss; all loss values are plotted to construct the 1D loss curve (as a function of the selected egomotion parameter). For the forward translation  $t_z$ , we generate  $N = 200$  uniformly sampled values in the range  $[t_z - 3t_z, t_z + 3t_z]$ . For the yaw (heading) angle, we generate  $N = 100$  uniformly sampled values in the range  $[\theta_y - 0.02, \theta_y + 0.02]$  radians. See Figure 7 for additional example loss surfaces. Here, we include illustrations of how the loss curves shift during the inference-time PFT. To generate these curves, we repeat this 1D loss curve generation procedure after every optimization epoch.

### A.2.2 Additional figures

We provide several more examples of our depth predictions, and the resulting error images in Figures 8 and 9. Additionally, we include some “failure modes” in Figure 10. Specifically, our optimization method occasionally removes thin objects (like poles or trees) and will shift moving objects in such a way that minimizes the loss, but does not represent reality. We aim to address these drawbacks in future work.

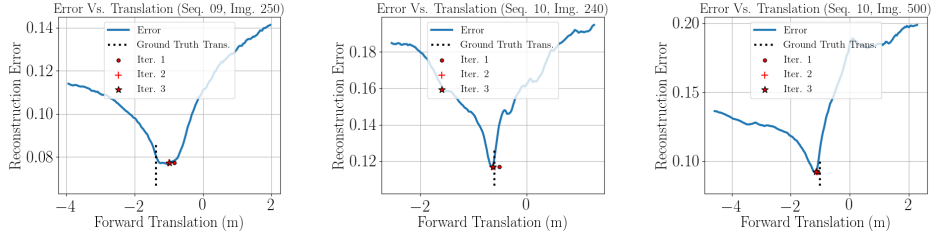
### A.2.3 Additional pose perturbation experiment details

In this experiment, we perturb the first iteration egomotion prediction by adding uniformly distributed noise to the translation and yaw values, and then proceed with additional iterations that take as input the (perturbed) warped source image. The initial pose perturbation causes the reconstruction image to become further away from the target image, which the subsequent iterations must correct for in order to re-align the warped source image with the target image. We show that despite the initial erroneous operating point, the subsequent forward passes through our network produce corrections that bring the egomotion prediction back to the minimum.

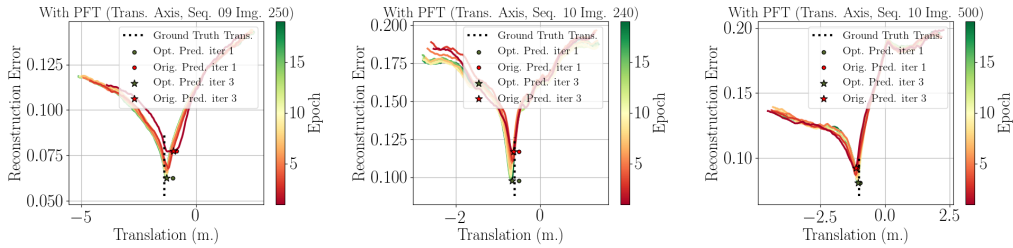
Concretely, we apply pose perturbations (in the forward translation direction, and along the yaw axis) to the initial egomotion prediction. The translation perturbation is sampled from a uniform distribution in the range  $[-\alpha, \alpha]$ , where  $\alpha \in \{0, 0.1, 0.25, 0.5, 0.75, 1.0, 1.5\}$  meters, and the yaw perturbation is sampled from a uniform distribution in the range  $[-\beta, \beta]$ , where  $\beta \in \{0, 0.1, 0.25, 0.5, 1, 3, 5\}$  degrees. A random perturbation is applied to every sample within KITTI test sequences 09 and 10, and we report the resulting errors in Figure 11. Here, we include the effects of applying translation and rotation perturbations independently, and then in combination. As a baseline, we report the error for our single iteration model with random noise added to its one-shot prediction (this is the error range we expect to see if our iterative network cannot correct for the added error).

### A.2.4 Additional depth scaling experiment details

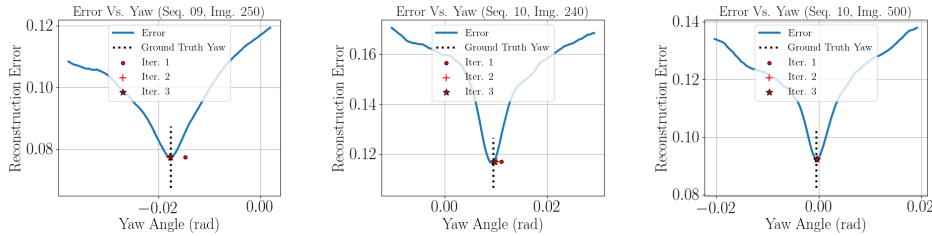
In this experiment, we simulate scale drift between the depth and egomotion networks by varying the scale factor  $s$  of the depth predictions ( $\mathbf{D}_{scaled} = s\mathbf{D}_{pred}$ ). We demonstrate that through the coupling of our networks (through iterative egomotion estimation), the scale drift is mitigated. In this experiment, we apply a scaling factor  $s \in \{0.7, 0.8, 0.9, 1.0, 1.1, 1.2, 1.3\}$  to all depth predictions in our test sequences. We compute the change in translation norm (relative to the translation norm with an applied scale factor of 1) of our iterative egomotion network predictions. As expected, the relative



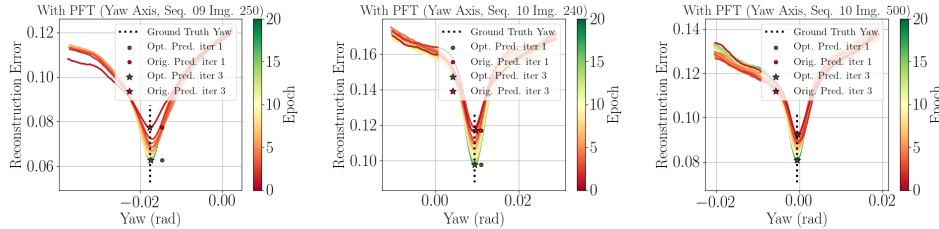
(a) 1D loss curves (in the forward translation axis) generated using the original (non-optimized) depth network prediction



(b) 1D loss curves (in the forward translation axis) showing improved convergence due to the refined depth prediction as a result of using our PFT strategy.



(c) 1D loss curves (in the yaw axis) generated using the original (non-optimized) depth network prediction



(d) 1D loss curves (in the yaw axis) showing improved convergence due to the refined depth prediction as a result of using our PFT strategy.

Figure 7: 1D loss surface experiment demonstrating that the iterative egomotion prediction converges to minimum of the loss function, and inference-time PFT of the depth network further minimizes the overall loss curve.

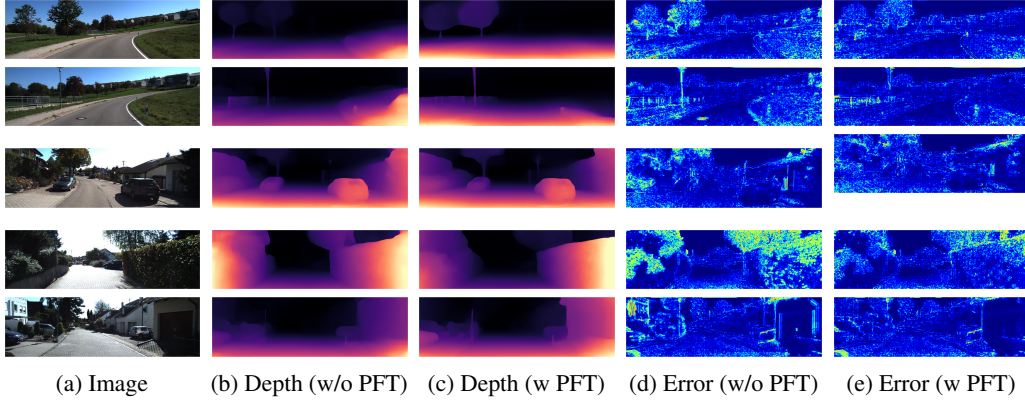


Figure 8: Additional depth predictions for KITT dataset images. We show the original network prediction, and the optimized result after applying our PFT strategy

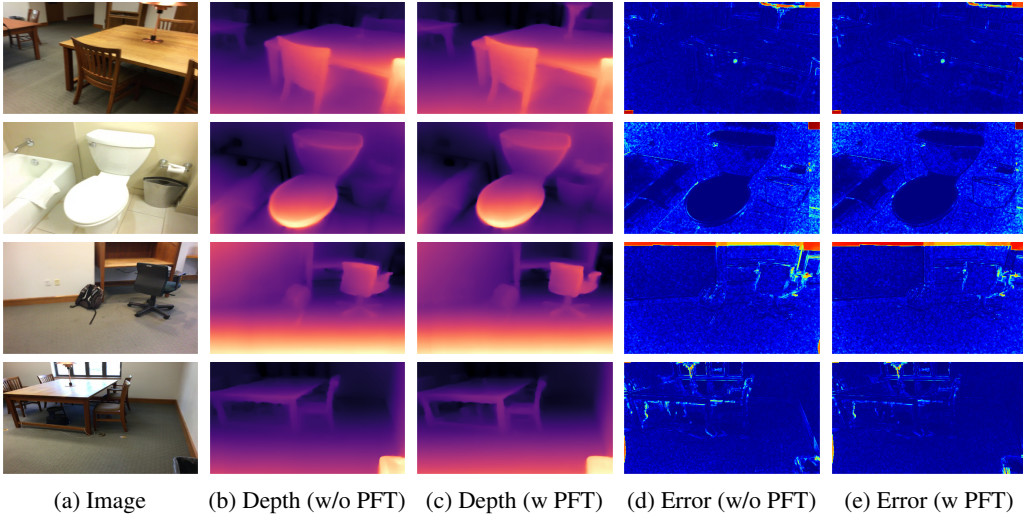


Figure 9: Additional depth predictions for ScanNet dataset images. We show the original network prediction, and the optimized result after applying our PFT strategy.

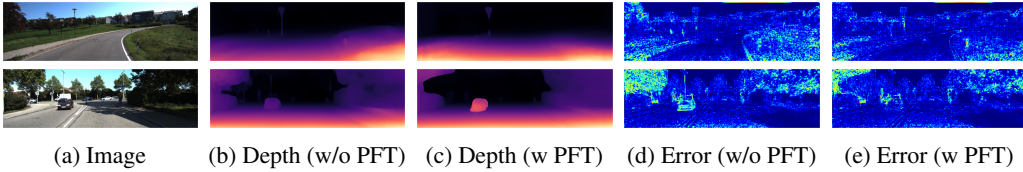


Figure 10: failure mode examples for our PFT strategy: in the first case, some thin objects are removed; in the second case, the optimization shifts the car's depth closer to the camera to account for its forward motion

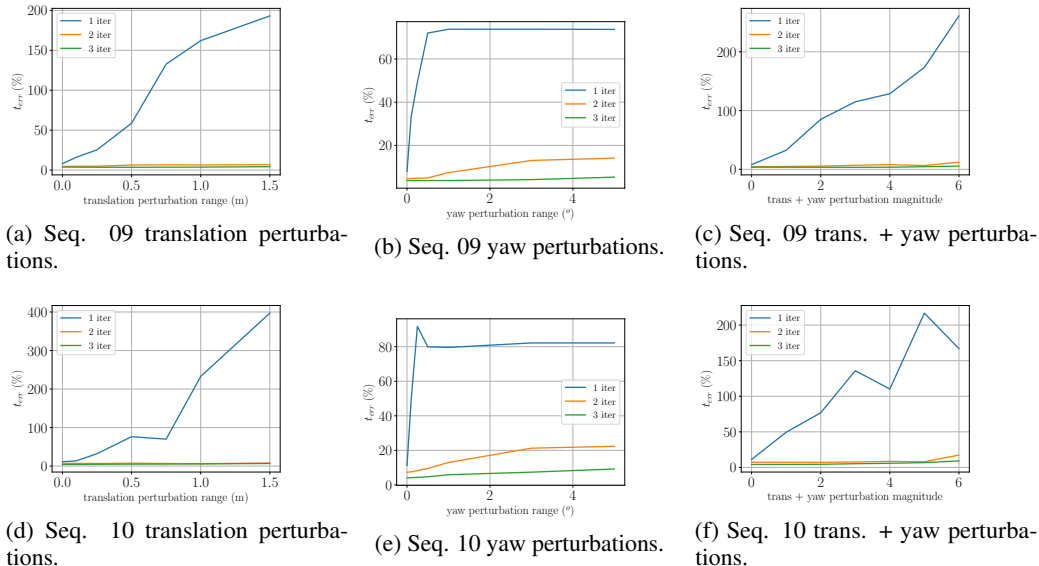
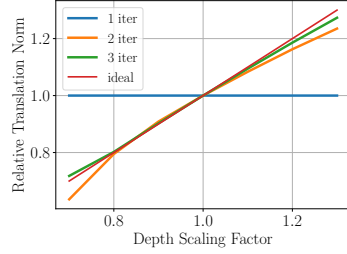


Figure 11: Full results for the pose perturbation experiments. Through coupling, our iterative egomotion network can account for large pose perturbations that would otherwise degrade the egomotion accuracy.

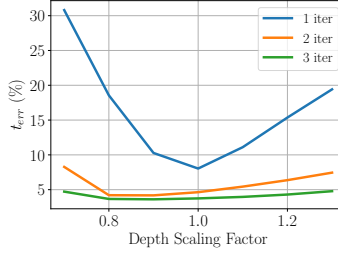
change in the predicted translation norm is approximately equal to the depth scaling factor. We report this result Figures 12a and 12b. In Figures 12c and 12d we also apply the same scale factor to the ground truth position values, and report the  $t_{err}$  between our predictions and the rescaled ground truth. With our iterative method, we see that the error remains relatively constant. In contrast, without being able to account for the depth scale drift with the single iteration network, the error increases with the magnitude of the scale drift, since the egomotion prediction remains fixed while effective ground truth motion changes as the scene depth is rescaled. Note that in this experiment, we do not apply any scale alignment using ground truth, since this would account for the scale inconsistency by utilizing ground truth information. Instead, we use the online rescaling approach ([47]) to rescale the egomotion predictions based on the observed camera height (compared with the known camera height) prior to reporting the translation error.

### A.2.5 KITTI Depth Ablation

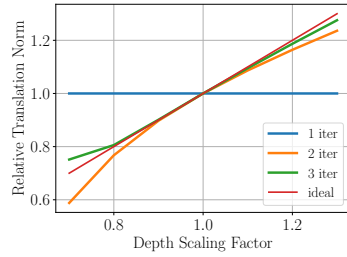
Table 11 provides an ablation study for the depth evaluation on the KITTI (Eigen) test split. We see that applying PFT leads to an improvement in all cases, and is more effective than applying iteration in this case. This differs from our ablation study on ScanNet, where we see that iteration is crucial for improving accuracy. We postulate that this is due to the camera motion being more constrained for KITTI compared with ScanNet; the 6-DOF camera pose changes of ScanNet are more difficult to learn than the more simple forward motion of the KITTI dataset. This simplified motion allows our one-iteration egomotion network to achieve a high level of accuracy, and as a result causes additional iterations to not have a significant amount of impact. In contrast, due to the complexity of motion within ScanNet, more iterations are required to improve generalization of the egomotion network (which is crucial to have for refining depth predictions via PFT).



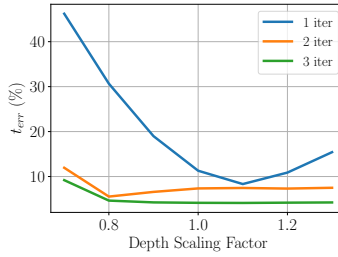
(a) Seq. 09. relative translation norms.



(b) Seq. 09. translation error



(c) Seq. 10. relative translation norms.



(d) Seq. 10. translation error

Figure 12: Full results of the depth scaling experiment. The iterative egomotion network can accurately account for the change in scale of the depth prediction.

Table 11: Ablation study for the KITTI Eigen test split. As the number of egomotion optimizer iterations increases, the accuracy after test-time depth optimization increases.

# Egomotion Iter.	Test-time Depth Opt.	Error ↓				Accuracy ↑		
		Abs Rel	Sq Rel	RMSE	RMSE log	$\delta < 1.25$	$\delta < 1.25^2$	$\delta < 1.25^3$
1	—	0.123	0.934	4.990	0.200	0.860	0.956	0.980
2	—	0.119	0.934	4.959	0.197	0.868	0.957	0.980
3	—	0.119	0.929	4.935	0.197	0.868	0.957	0.980
4	—	0.117	0.954	4.902	0.196	0.870	0.958	0.981
1	$\theta_D + \theta_E$	0.099	0.784	4.460	0.179	0.896	0.963	0.982
2	$\theta_D + \theta_E$	0.097	0.774	4.440	0.178	0.899	0.963	0.982
3	$\theta_D + \theta_E$	0.095	0.769	4.414	0.177	0.902	0.963	0.982
4	$\theta_D + \theta_E$	0.094	0.783	4.391	0.176	0.903	0.964	0.982
1	$\theta_D$	0.108	0.822	4.583	0.186	0.883	0.959	0.981
2	$\theta_D$	0.099	0.785	4.473	0.182	0.890	0.958	0.981
3	$\theta_D$	0.098	0.775	4.410	0.180	0.894	0.960	0.981
4	$\theta_D$	0.097	0.781	4.385	0.178	0.897	0.961	0.982